Advanced Functional Materials

ADVANCED FUNCTIONAL MATERIALS
www.afm-journal.de

RESEARCH ARTICLE OPEN ACCESS

Parallel 3D Bioprinting on SLIPS-Microarrays

Julius von Padberg[1] | Julian A. Serna[1] | Maike Schliephake[1] | Pavel A. Levkin[1,2]

[1]Karlsruhe Institute of Technology (KIT), Institute of Biological and Chemical Systems – Functional Molecular Systems (IBCS-FMS), Kaiserstraße 12, Karlsruhe, Germany | [2]Karlsruhe Institute of Technology (KIT), Institute of Organic Chemistry (IOC), Kaiserstraße 12, Karlsruhe, Germany

Correspondence: Pavel A. Levkin (levkin@kit.edu)

Received: 21 November 2025 | **Revised:** 15 March 2026 | **Accepted:** 25 March 2026

Keywords: 3D bioprinting | high-thoughput screening | parallelization | slippery liquid-infused porous surface | wettability patterning

ABSTRACT

Parallelization remains a key challenge in advancing three-dimensional (3D) bioprinting from a prototyping method to a practical tool for true high-throughput screening (HTS). HTS requires arrays of physiologically relevant 3D tissue models that remain viable under immersion in liquid. Yet current 3D bioprinting on liquid compartmentalization platforms is inherently serial. Sequential fabrication scales unfavorably with the array sizes required for ever-growing libraries in disease modeling and drug discovery, forcing a trade-off between physiological relevance and throughput. Here, we present a parallel 3D bioprinting solution that integrates Digital Light Processing (DLP) stereolithography with a wettability-patterned slippery liquid-infused porous surface (SLIPS) - Droplet Microarray (DMA). This wall-less compartmentalization platform repels gelatin methacryloyl (GelMA) inks and maintains stable droplet boundaries, enabling complete postprinting immersion of hydrogel structures in liquid droplets. By eliminating the physical solid walls between compartments, it becomes possible to fabricate arrays of 3D hydrogel structures in parallel, effectively decoupling fabrication time from array size. Thus, this work bridges the gap between 3D tissue-model arrays and fabrication speed required for HTS. Using optimized printing parameters, we fabricate tens to hundreds of cell-laden GelMA structures within 10 min, preserving cell viability and compartmentalization. Our parallel 3D printing– SLIPS–DMA approach establishes a flexible system-on-a-chip for miniaturized multicondition HTS of cell–material–drug interactions.

1 | Introduction

Three-dimensional (3D) biofabrication has become a central technology in tissue engineering, personalized medicine, and drug discovery, where 3D cell models immersed in liquids simulating the in vivo environment are essential for studying complex biological responses. Modern approaches such as 3D bioprinting, enable the creation of tissue-like structures with controlled architecture and composition. Despite these advances, 3D bioprinting remains limited due to its inherent sequential nature, where structures are fabricated one after another, severely limiting throughput and scalability. Consequently, high-throughput screening (HTS) in these fields is primarily conducted using 2D cell cultures due to their rapid fabrication speed [1–3]. This comes at the cost of physiological relevance, as 3D culture provide a more accurate in vivo representation [4–6], creating a fundamental trade-off. As a result, fabricating an array consisting of many individual cell-laden 3D structures immersed in separate compartmentalized liquids at a throughput suitable for HTS applications poses a significant challenge.

One root cause of the challenge lies in the need for the compartmentalized liquid volumes surrounding the 3D biofabricated structures. Compartmentalization has conventionally relied on physical walls, but these barriers impede print-head movement and force sequential traversal between compartments [7–11] (Figure 1C).

The general throughput of HTS was increased through miniaturization moving from few-well plates to higher numbers of wells

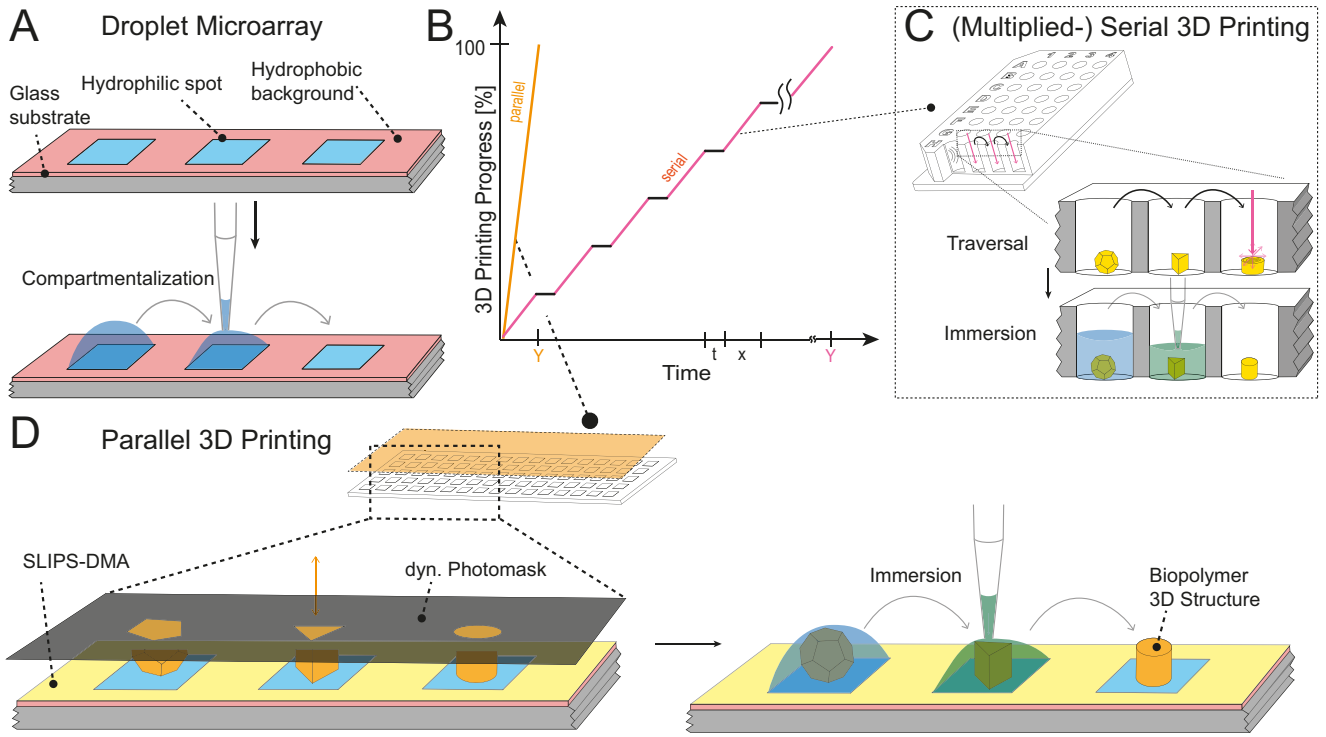

FIGURE 1 | Concept of parallel 3D biofabrication on the slippery liquid-infused porous surface (SLIPS)–DMA platform. (A) Schematic of the Droplet Microarray (DMA) platform consisting of hydrophilic spots on a superhydrophobic background, enabling wall-less liquid compartmentalization through high local wettability contrast. (B) Comparison of serial versus parallel 3D bioprinting workflows. In serial systems, print time (Y) scales linearly with the number of compartments (x) due to intercompartment traversal (t), whereas in parallel fabrication, all structures are printed simultaneously, maintaining constant fabrication time independent of array size. (C) Conventional compartmentalization using physical walls, which restricts printhead motion dictating the use of serial 3D printing technology following the platform's layout. (D) Schematic of the developed SLIPS–DMA platform enabling parallel DLP-based 3D bioprinting of hydrogel structures directly onto hydrophilic spots. The SLIPS treatment maintains droplet-based compartmentalization during printing (left) and allows subsequent full immersion of the printed structures in defined liquid environments (right).

per plate. Thus, required volumes for screenings saw a significant reduction with the density of wells per platform increasing. With a higher density of experiments per area, simpler parallelization of these experiments was in turn enabled by processing the whole substrate with 3D tissues at the same time. Conclusively, in HTS of 3D tissue substitutes on liquid compartmentalization platforms, parallelization has been implemented at the platform level [12], but fabrication continues to be serial [9–11]. As a result, with the number of compartments per platform increasing, the total print time including both structure fabrication and intercompartment traversal scales unfavorably (Figure 1B), resulting in a contradictory low throughput. To exploit the higher compartment density enabled by miniaturization, all structures must be fabricated simultaneously. In this work, we selected parallel layer-wise depositing Digital Light Processing (DLP) stereolithography to realize this goal. This technology is capable of independent fabrication across the entire printing area, allowing simultaneous printing of an array of 3D tissue substitutes. A multiprinthead serial setup could theoretically achieve this but would be too complex and require layout-specific solutions, rendering it economically impossible for most cases. In contrast, DLP is only constrained by pixel size and the size of the overall printing area [13, 14]. In DLP, a dynamic photomask is projected into a vat containing photopolymerizable ink, cross-linking the whole layer defined by the projected image. Repeating this process sequentially builds the varying cross-sections of the structures. As long as the array fits within the projection area, multiple structures can be fabricated simultaneously [15] (Figure 1D).

To use parallel fabrication technology to the full extent, all compartments must be accessible simultaneously without obstacles between individual structures. This requires a platform capable of compartmentalizing liquids without relying on solid physical walls to separate each compartment. By combining such a physical wall-less platform with parallel 3D printing technology, intercompartment travel (t) could be eliminated. Utilizing parallel technology would reduce total fabrication time (Y) for the array to a fraction of that required in a serial printing process, equaling the time needed to print a single structure (x, Figure 1B).

A platform that meets these requirements for high-throughput 3D biofabrication, overcoming aforementioned geometric and mechanical limitations is the Droplet Microarray (DMA), developed in our group [16–21]. It is a liquid compartmentalization platform based on a surface-patterned glass slide, consisting of hydrophilic spots separated by a superhydrophobic background (Figure 1A). The high local contrast in wettability is used to compartmentalize liquids into stable droplets without solid walls separating them [22–26].

These hydrophilic spots serve as target locations for 3D printing of individual structures. By designing the 3D models to partially cover hydrophilic spots, it is possible to completely immerse them in liquid droplets confined by the borders after 3D printing (Figure 1D). This allows combinations of different liquid media and hydrogel compositions to be screened as cell or tumor environments. Achieving such structures on the DMA without 3D printing would require complex molds with undercuts requiring lost form casting, both of which are time-consuming and labor-intensive [27]. Parallel 3D bioprinting offers efficient and straightforward implementation of changes to the hydrogel's geometry between prints and thereby the ratio of liquid environment to structure volume. This could enable controlled modulation of the exchange rate of nutrients and waste between gel and the surrounding media.

In this work a synergistic system enabling combinatorial use of both technologies was iteratively optimized and manufactured by rapid prototyping. Leveraging this developed system, we present a process that combines the speed advantage of parallel 3D biofabrication technology with a miniaturized high-density wall-less liquid compartmentalization platform. To achieve this, we combined parallel projection stereolithography using DLP with the DMA as solid wall-less liquid compartmentalization platform.

Introducing the wettability-patterned platform to complex biopolymer-based hydrogel ink during 3D printing poses a challenge. The biopolymers can act as mild surfactants, wetting superhydrophobic surfaces and bind nonspecifically to them, resulting in the loss of compartmentalization of the DMA.

To overcome this limitation, here we introduce a slippery liquid-infused porous surface (SLIPS) to create ink and hydrogel-repellent regions between the hydrophilic spots [28, 29]. The resulting SLIPS–DMA platform consists of a porous superhydrophobic coating impregnated with repellent perfluorinated oil. The retained oil in the nanopores creates a stable lubricating layer that prevents wetting by low-surface-tension inks. This design uniquely enables parallel 3D printing with biopolymer-based hydrogel inks directly onto the hydrophilic spots while maintaining robust droplet-based compartmentalization following the printing step. It also allows full immersion of the 3D printed structures for downstream high-throughput experiments (Figure 1D).

2 | Results & Discussion

2.1 | Characterization and Fabrication of SLIPS–DMA as Build Surface for Parallel 3D Bioprinting

We found that native DMA surfaces lose compartmentalization when exposed to gelatin methacryloyl (GelMA) inks. During the development of a setup that enabled 3D printing on patterned DMA substrates, we carried out initial test prints on a DMA with 672 square hydrophilic spots (1 mm edge length) to evaluate surface compatibility. An array of 3D structures made of synthetic ink based on polyethylene glycol diacrylate (PEGDA) could be printed without loss of functionality. However, when attempting to immerse 3D printed pyramids (500 µm characteristic length) made from functionalized natural biopolymer GelMA on a similar native DMA, the surface wetting behavior changed. Even on the superhydrophobic background, water completely wetted the surface between the structures, forming liquid bridges between spots (Figure 2C(A)). We attribute the dominant cause of the loss of compartmentalization to reduced background hydrophobicity. Biomaterial inks comprised of complex biopolymers like GelMA in solution are likely to adhere through forces like London dispersion forces, which increase with molecular size. Consequently, GelMA in solution can adhere to both the hydrophobic background and the hydrophilic spots reducing the surface-energy contrast. This interaction compromises one of the core functions of the DMA for droplet stability. The compartmentalization loss prevents complete immersion of the 3D printed hydrogel structures. Residual surface tension retained small liquid volumes around the structures (Figure 2C(A)). However, this is insufficient for full immersion (Figure 2C(C)), which is essential for consistent exposure for downstream high-throughput screening applications. To restore compartmentalization, it is imperative to prevent adherence of the biomaterial ink to the DMA surface.

To further investigate GelMA exposure as the cause of the loss of compartmentalization, a superhydrophobic (SH) slide underwent a simulated 3D printing process with the water contact angle (WCA) serving as quantitative measure of the change in wetting behavior. The SH slide was exposed to a 10% w/v GelMA ink, solubilized in phosphate buffered saline (PBS), for 10 min and subsequently washed in PBS for 20 min. Consequently, the mean static WCA (θ_m) on the SH surface decreased significantly from $\theta_m = 156.7°$ to $\theta_m = 106.2°$ after GelMA exposure and washing (Figure 2A). We attribute the observed loss of compartmentalization to a transition of the Cassie–Baxter [30] to a Wenzel wetting state [31] induced by GelMA adsorption. The hydrophilic collagen domains in GelMA orient toward the liquid–air interface [32, 33], lowering the surface tension of the solution. This allows the liquid to invade the air pockets along the three-phase contact line, collapsing the Cassie–Baxter state into a Wenzel state, resulting in complete wetting of the surface. When observing a single droplet of the GelMA ink on the SH surface, the lower mean static contact angle (θ_{st}) exemplifies the described wetting behavior ($\theta_{st} = 130°$; Figure 2B(A)) compared to deionized water on the same surface ($\theta_m = 156.7°$; Figure 2A). Additionally, the roll-off angle (α) of $\alpha = 65°$ (Figure 2B(B)) indicates adherence of the GelMA ink to the surface following collapse of the Cassie–Baxter state. Even after the main droplet of ink rolled off, residual smaller droplets remained, confirming adherence to the SH surface (Figure 2B(C)).

This interpretation is supported by advancing WCA (θ_a) measurements (Figure 2F). To account for surface heterogeneity the advancing WCAs were determined in two replicate measurements (θ_{a1}, θ_{a2}), as detailed in Methods. Advancing WCAs of untreated superhydrophobic slides were consistently high ($\theta_{a1} = 153.0°$, $\theta_{a2} = 152.2°$, Figure 2F(A) with an average roll-off angle of $\alpha = 1.6°$ but dropped remarkably after 10 min GelMA ink exposure and 20 min of washing in warm PBS without any roll-off ($\theta_{a2} = 135.0°$; Figure 2F(B), measurement details in Methods). Following the trend of the first reported drastic increase of the roll-off angle of GelMA ink on the slide, the water droplet on an ink exposed surface after washing (Figure 2F(B1)) was completely pinned, even when tilted to 90° (Figure 2F(B2)).

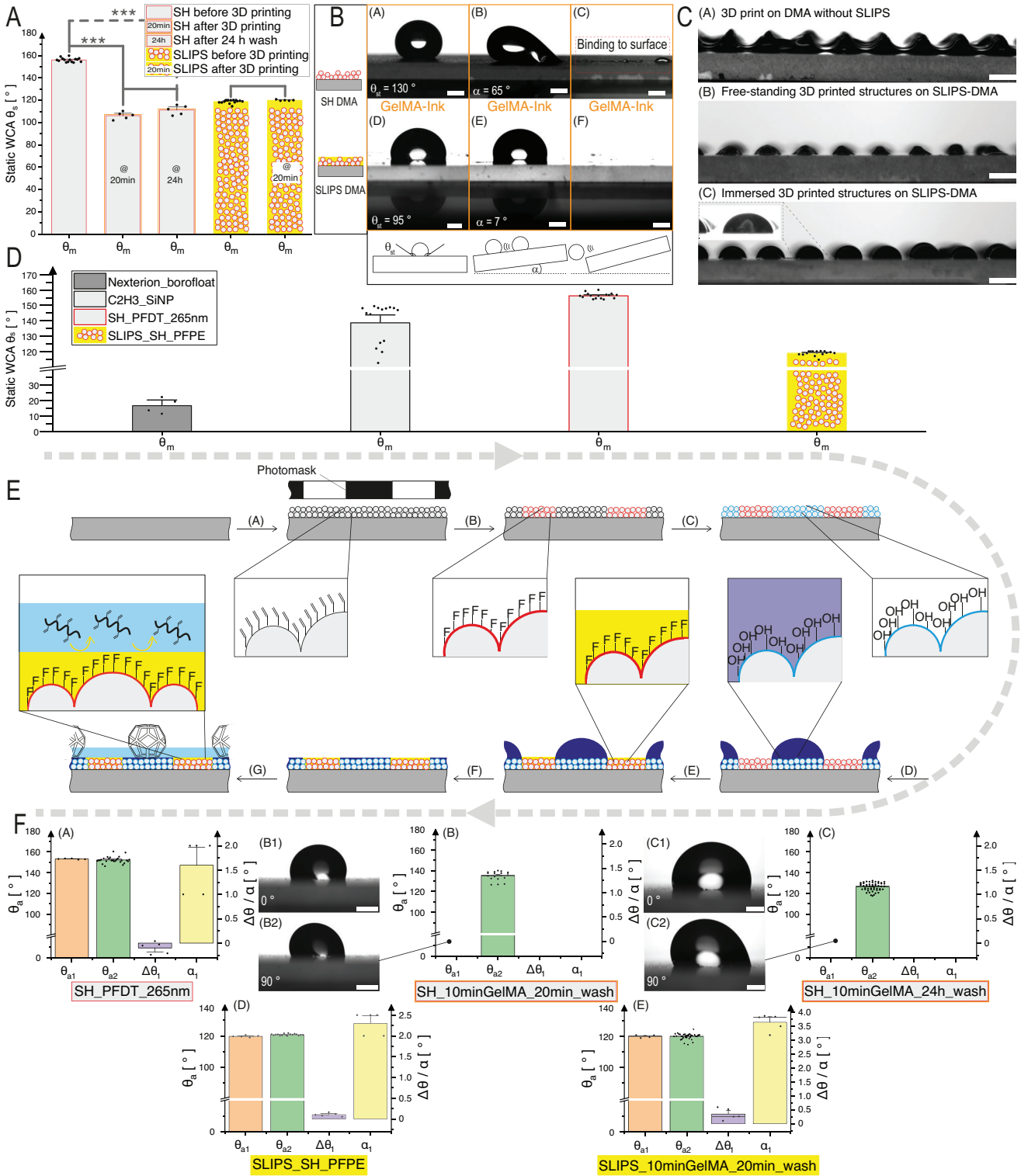

FIGURE 2 | (A) Mean static WCA (θ_m) comparison of SH and SLIPS surfaces before and after undergoing a simulated 3D printing process of 10 min GelMA exposure and 20 min washing in PBS to investigate the cause of the loss of compartmentalization capabilities on the untreated DMA after parallel 3D printing of biopolymer-based ink. (B) Comparison of wetting behavior of a droplet of 10% w/v GelMA ink in PBS on SH B(A–C) SLIPS surfaces B(D–F) in different states: static B(A/D), tilted B(B/E) and after contact B(C/F) and SLIPS surfaces. (C(A)), 3D printed GelMA hydrogel pyramids on an untreated DMA with 1 mm^2 cubical hydrophilic spots after printing with residual liquid around them. (C(B)) 3D printed GelMA hydrogel pyramids on a SLIPS–DMA without residual liquid around them. (C(C)) 3D printed GelMA hydrogel pyramids fully immersed in compartmentalized droplets on SLIPS–DMA, showing that the introduction of the SLIPS–DMA to GelMA ink successfully addresses the issue of nonspecific binding, which becomes pronounced with hydrogels formed from larger biopolymer molecules. The intended goal of being able to create 3D hydrogel structures of controlled geometry, that can be fully immersed in compartmentalized droplets became achievable. (D) Static WCA measurements recorded at each major step of the SLIPS–DMA manufacturing. (E) Workflow to create SLIPS–DMA. (F) Comparison of the advancing WCA, WCA hysteresis and roll-off angle on

To test whether GelMA molecules were nonspecifically binding to the surface, rather than forming a removable layer, slides were washed for 24 h after ink exposure. The contact angles were then remeasured. The mean static WCA did not increase significantly ($p > 0.05$) to $\theta_m = 111.2°$, remaining significantly decreased compared to before the exposure but hydrophobic ($p > 0.001$; Figure 2A). The persistence of the reduced static contact angle after 24 h of washing indicates that the reduced background hydrophobicity was not caused by removable physical residue blocking the nanopores. This conclusion is further supported by the results of the advancing contact angle measurements. For the prolonged washing time of 24 h, the determined advancing WCA is $\theta_{a2} = 126.1$ (Figure 2F(C)). Regardless of the washing time, after exposure to GelMA ink the advancing contact angle decreased drastically compared to before the exposure.

Qualitatively, the measurements behave similarly between sets of advancing and static WCAs, but after GelMA ink exposure and a 24 h washing period, a decrease in advancing WCA (Figure 2F(C)) compared to an increase in static WCA measurements (Figure 2A) can be observed. This specific behavior of the droplet on the surface can be caused by the removal of stronger pinning sites during long washing. The advancing WCA is more sensitive to the physical roughness and heterogeneity that causes pinning [34]. These pinning sites are responsible for the initially larger advancing WCA after 20 min of washing. They appear unaffected or less affected by the nonspecifically bound GelMA ink. After the prolonged washing period the pinning sites were then removed, resulting in a reduced advancing contact angle. The pinning sites interfere less with static droplets on heterogeneous surfaces, hence the overall smaller static WCA. The prolonged washing could have caused the slight removal of potentially remaining GelMA ink residue, and thereby the increase in the static WCA.

In conclusion, independent of the washing duration, the exposure of the porous SH surface to GelMA ink resulted in a reduced static WCA and a dramatically changed dynamic wetting behavior. In the case of the DMA the advancing contact angle is a crucial surface characteristic, as it is the determining factor of the maximum compartmentalizable volume in the droplets on the DMA.

The functionalized nanoporous architecture of the DMA presents a challenge when in contact with surfactants such as complex biopolymers in hydrogel inks. The large surface area increases the likelihood of adherence, but it is essential for maintaining large contact angle contrast required for reliable compartmentalization. Solutions must preserve droplet compartmentalization and nonspecific binding must be prevented. Intriguingly, the porosity, can be exploited by selectively infusing the surface with a lubricating liquid to create a slippery interface [28, 35, 36]. This allows hydrogel repellency, while preserving the system's droplet-forming capacity. This setup leverages the low adhesion of the biomaterial ink to the SLIPS, as shown by a decrease in the roll-off angle (α) of GelMA ink on the SLIPS slide from 65° (Figure 2B(B)) to 7° (Figure 2B(E)). The low-adhesion property is achieved while maintaining a static WCA above 90°, rendering the surface hydrophobic (Figure 2B(D)). Furthermore, it effectively preserves the slide's compartmentalization capability (Figure 2C(C)) through prevention of the binding of GelMA ink to the surface after contact (Figure 2C(B)), rendering it hydrogel-repellent. No visible ink residue remains on the surface after being exposed to the GelMA-based hydrogel inks (Figure 2B(F)).

The combination of a pattern of locally different wettabilities and hydrogel repellency is achieved by following the previously developed protocol [28, 29]. The foundation for the subsequent steps is a hydrophilic glass substrate ($\theta_m = 16.6°$; Figure 2D). First, the slides are exposed to ozone to activate the surface for chemical bonding. This process also removes organic contaminants through oxidization. During activation the substrate is enriched with reactive hydroxyl groups on the surface (Figure 2E(A)).

Next, a vinyl–silica solution is spin-coated on the slides. The coating creates a nanoporous surface with attached nonpolar vinyl groups ($\theta_m = 138.7$; Figure 2D). Thiols containing functional moieties can be selectively attached through a photomask. At exposed locations, the surface-attached vinyl groups react with the thiols through a thiol-ene photoclick reaction (Figure 2E(B)). The combination of highly nonpolar tail groups and the nanoporous surface results in superhydrophobicity ($\theta_m = 156.2°$; Figure 2D). To create high contrast in local wettability, the previously unexposed locations are now functionalized through another thiol-ene photoclick reaction using mercaptoethanol. Highly polar hydroxyl groups are attached to the nanoporous surface in these spots to achieve ultralow contact angles in the range of superhydrophilicity ($\theta_m < 10°$) (Figure 2E(C)).

With the DMA fabricated, the patterned SLIPS can be created. Therefore, stable water droplets are formed on the hydrophilic spots to prevent them from being flooded by the slippery liquid (Figure 2E(D)). With the hydrophilic spots blocked, the

an SH and a SLIPS slide before F(A/D) and after simulated 3D printing process F(D/E) and after a prolonged 24 h washing period of the SH slide after GelMA exposure to proof adherence of GelMA to the surface rather than a loosely attached physical layer blocking the surface F(C). Advancing contact angles were determined through the tilting plate method and validated through the syringe method, denoted as θ_{a1} and θ_{a2}, respectively. In a few cases on GelMA-exposed superhydrophobic slides, strong local pinning led to asymmetric droplet motion, with the pinned contact angle occasionally exceeding the advancing one. The potential mechanisms underlying this behavior are discussed in the Supporting Information. In the cases of the SH surface after simulated 3D printing, the droplets were completely pinned, no matter the roll-off angle F(B1/B2) or the washing duration F(C1/C2). All scalebars represent 1 mm. Differences in mean static WCA were assessed using paired *t*-tests ($p \leq 0.05$; ***, **, * indicate $p < 0.001$, 0.01, 0.05). Sample sizes were $n = 15$ for untreated SH and SLIPS surfaces, $n = 5$ for postprinting and 24 h washing conditions, and $n = 4$ for hydrophilic glass. All bar charts represent the mean (bar height) with the median indicated as a horizontal line; error bar shows +1.5 × standard error of the mean (SEM). Individual data points are overlaid to display measurement variability. A tabulated overview is depicted in the Supporting Information.

porous superhydrophobic background is immersed in perfluoropolyether (PFPE) oil (Figure 2E(E)). The hydrophilic spots remain stable, flooded with water. Without the water, the high surface energy of the spot would attract the low surface tension PFPE oil and allow it to spread. The immersion reduces the surface's wettability from superhydrophobicity to hydrophobicity ($\theta_m = 118.9°$; Figure 2D). This value is consistent with previously reported contact angles for a similar SLIPS surface [37]. To prepare the SLIPS–DMA for printing, the droplets on the surface are evaporated. This is done either by exposing the slide to a dry air environment or more rapidly by placing it on a heated plate (Figure 2E(F)). To maintain the integrity of the hydrophilic spots, it is necessary to prevent oil intrusion from the adjacent superhydrophobic background. Consequently, complete evaporation of water in the nanopores must be prevented. Although this was not observed even after multiple days, it remains a potential phenomenon to consider.

With the SLIPS–DMA fully prepared, it can be used for parallel 3D printing of inks with large biopolymer molecules by preventing nonspecific binding to the superhydrophobic background (Figure 2E(G)). These long polymer chains would have bound nonspecifically through forces like London dispersion forces, which grow with the molecular chain length.

To verify the biopolymer ink-repellent behavior of the fabricated SLIPS DMA, we examined its interaction with GelMA hydrogel ink under identical simulated printing conditions to those applied to the SH slide. An unpatterned SLIPS slide was exposed to GelMA biomaterial ink for 10 min and subsequently washed in PBS for 20 min. The mean static WCA before exposure ($\theta_m = 118.9°$, Figure 2A) did not change significantly ($p > 0.05$) after exposure and washing ($\theta_m = 120.1°$, Figure 2A), confirming that GelMA was effectively repelled. The slight increase after washing can be attributed to the removal of physical contaminants from the surface.

The advancing WCA θ_a remained largely unaffected by exposure to GelMA on the SLIPS-surface before($\theta_{a1} = 119.7°$, $\theta_{a2} = 120.7°$, Figure 2F(D)) and after exposure ($\theta_{a1} = 120.1°$, $\theta_{a2} = 119.9°$, Figure 2F(E)) further supporting the claimed repellency. However, exposing the SLIPS slide to GelMA resulted in a slight increase in roll-off angle (α)($\alpha = 2.3°$, $\alpha = 3.6°$, before and after GelMA exposure, respectively) and the corresponding expansion of the WCA hysteresis ($\Delta\theta$). Before GelMA exposure, the hysteresis was comparable ($\Delta\theta_1 = 0.1°$) to the hysteresis of the superhydrophobic surface ($\Delta\theta_1 = -0.1°$). After GelMA exposure, the WCA hysteresis increased slightly ($\Delta\theta_1 = 0.3°$). Nevertheless, compared to the SH surface after GelMA exposure, where water droplets were fully pinned at 90° tilt, SLIPS preserved droplet mobility, highlighting the GelMA repellency. The observed increase in hysteresis in combination with the broader distributed advancing contact angles suggests a partial loss of PFPE oil during extended washing. Shorter washing times that only remove the un-cross-linked ink may counteract this effect. Overall, the contact angles remained stable before and after exposure, with no significant deviation between the measurements, confirming the hydrogel-repellent properties of the SLIPS surface and its suitability for maintaining compartmentalization during 3D bioprinting.

2.2 | System & Process Engineering

The objective was to effectively integrate two existing systems: parallel DLP technology for 3D bioprinting of cell laden hydrogel structures and the DMA for immersion in stable, compartmentalized liquid droplets. Therefore, a new interfacial system combining both had to be engineered. Concept variants were designed, realized through prototypes and iteratively refined to ensure optimal functionality and efficiency.

At the end of this iterative optimization process, a system compatible with both the commercial DLP 3D bioprinter (LumenX+, Cellink) and the DMA was developed. The system consists of a spring-loaded two-part fixture, mounted on a carrier which connects it to the printer's z-axis (Figure 3D). The DMA is inserted into one half of the fixture and positioned against a perpendicular corner, formed by two reference shoulders. When fully inserted, the opposing half encloses the slide to secure it in place. A clamping force is applied by two coil compression springs, pushing the two halves of the fixture together. Threaded bolts running through each coil spring allow adjustment of the compressive preload via corresponding threaded nuts. The fixture is mounted to a linearly guided carrier to prevent rotation around the z-axis. The carrier mechanism can be locked after leveling, while the fixture can be pivoted to align the DMA parallel to the projection screen in the unlocked state. During the leveling, the DMA in the fixture is pressed against the PDMS-coated VAT-bottom. Once parallel, the four bolts are used to lock the position of the fixture in place. This procedure expels the air between the bottom of the vat and the DMA, creating a vacuum that resists the upward movement of the z-Axis. To prevent removal of the DMA from the fixture, vacuum channels are integrated and sealed through O-rings against the back of the slide. After insertion and centering, vacuum is applied to securely hold the DMA throughout the subsequent steps of the process.

The developed system enabled simple insertion, secure retention, and seamless removal of the DMA slide, while ensuring repeatable centering and guaranteeing parallelism with the projection plane. Therefore, it can operate as the interface between the commercial bioprinter and DMAs, thus enabling parallel DLP-based 3D printing directly onto the slide. In consequence, a process based on the established 3D printing methodologies was established. This new approach allows 3D bioprinting on all hydrophilic spots of the DMA at once. Similarly to known 3D printing processes, it can be divided into preprocessing, processing, postprocessing [38]. All necessary steps are depicted in Figure 3.

During the printing preparation, the desired 3D model is first designed in a computer-aided design (CAD) software. Individual models are then placed, oriented and positioned within an assembly that matches the chosen DMA layout (Figure 3A). Printing parameters such as exposure times (base-/ and body-layer) as well as lift and retracting speeds can be defined. The selected biomaterial ink may require preparation before use, for example heating to avoid thermoreversible gelation. To generate a bioink, cellular or bacterial material has to be mixed with the biomaterial ink (Figure 3B). Depending on the type of material, different preparations are required as described in the Methods section.

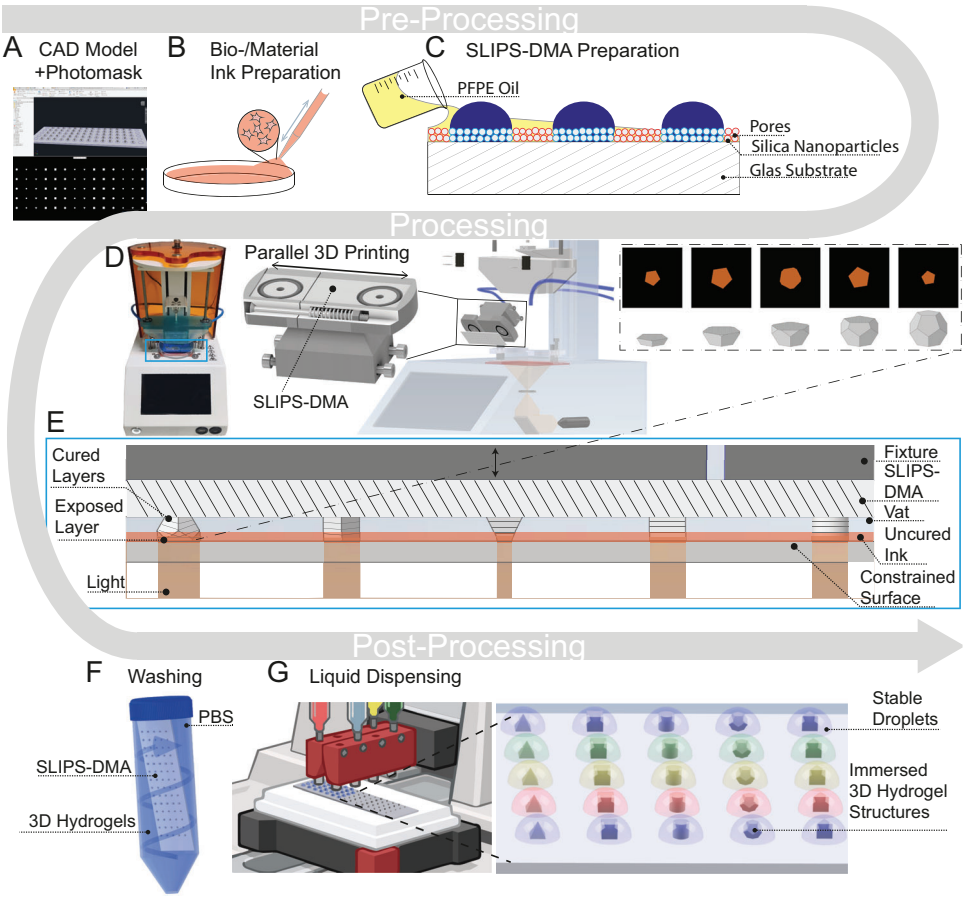

FIGURE 3 | Workflow of the parallel DLP-based 3D bioprinting system integrated with DMA. (A) Design and placement of individual 3D models in CAD (top) according to the DMA layout and subsequent printing parameter definition in the slicer program (bottom). Each structure is positioned to match a hydrophilic spot on the platform and printing parameters are defined for optimal shape fidelity according to the selected biomaterial or bioink containing cells. (B) Preparation of bioinks through combination of biomaterial inks with cellular or bacterial components; heating or other treatments are applied where required to ensure appropriate viscosity and prevent premature gelation. (C) Transformation of the DMA into a SLIPS–DMA by infusion with PFPE oil of the nanoporous superhydrophobic background generating ink- and hydrogel-repellent regions between hydrophilic spots. (D) Insertion of the DMA into the developed spring-loaded fixture and subsequent mounting of the assembly on the developed printer's *z*-axis carrier. The two-part assembly securely holds, centers and levels the DMA slide against the PDMS-coated vat. (E) Schematic of the parallel DLP printing process. Layer-wise projection of a dynamic binary photomask enables simultaneous cross-linking of all structures within the projection area (bottom). Cross-linking of a layer, peeling and recoating is repeated, until the tallest structure within the array is completed (top). (F) Postprinting washing procedure to remove un-cross-linked ink and residual material from the SLIPS–DMA surface and printed constructs, yielding clean, free-standing hydrogel structures. (G) Automated multiplexed liquid dispensing enables loading of different media or reagents into individual droplets for subsequent HTS (left). Final state of the printed array on the SLIPS–DMA. Each construct resides on a hydrophilic spot surrounded by compartmentalized liquid droplets, allowing complete immersion of the structures and enabling downstream high-throughput biological assays across combinations of different liquid media and hydrogel compositions that model distinct cell or tumor environments (right).

The DMA [21] as build surface is prepared and transformed into a SLIPS–DMA [29]. (Figure 3C).

The SLIPS–DMA is inserted into the fixture, which holds and centers it collinearly with the central axis of the vat. After insertion of the slide, the sliced model file is selected for printing and the levelling procedure can be performed. To print the base layer, the build surface is lowered into the ink one layer height above the constrained surface. The 3D printer simultaneously projects the individual cross sections in the ink. Upon light exposure, the functionalized biomaterial ink cross-links, forming the first layer between the two surfaces. The cross-linked layer is peeled from the constrained surface by lifting the carrier-fixture-DMA assembly along the *z*-axis. To cross-link the subsequent layers, the build surface is then lowered back into the ink, increasing the distance from the constrained surface by one additional layer height. This cycle is repeated until the tallest structure in the array is completed (Figure 3E). Since the binary dynamic photomask projects all distinct cross sections simultaneously, the total process time is solely determined by the maximum structure height.

Once the printing process has finished, the SLIPS–DMA with 3D printed structures on it, can be removed. Typically, each structure was designed to not completely cover the hydrophilic spot on the DMA. This partial coverage, combined with the gradient of cross-linking, decreasing toward the build surface, results in un-cross-linked ink around the structures and trapped

with each layer. In order to separate cross-linked structures from un-cross-linked ink, a washing step is required (Figure 3F).

Following the washing step, the clean, free-standing structures spots remain partially covering the hydrophilic spots. Together with the pronounced wettability contrast between spot and background, this enables the compartmentalization of liquids around the structures and subsequent complete structure immersion upon liquid dispensing (Figure 3G). The integration of parallel printing with wall-less liquid compartmentalization combined with automated handling technology establishes the process foundation for downstream high-throughput experiments on the platform.

2.3 | Printing Parameter Optimization

Depending on the ratios of photoabsorber, photoinitiator, and base material, the printing parameters must be fine-tuned for optimal shape fidelity of 3D printed structures on the platform [39–41] These printing parameters include layer height, base and body layer exposure time and in some cases retract speed of the printer's base plate [42].

The printing parameters for 10% w/v bovine GelMA solubilized in PBS 1X were optimized by comparing the printed characteristic length to the intended dimensions of the structures. Cubes of 0.125 mm^3 were chosen as test shape to simplify handling and maximize measurement consistency. Layer heights of 100 and 50 µm were chosen and the resulting 3D prints were evaluated (Figure 4A 50µm, Figure 4B 100 µm, respectively). Analysis of the measurements shows that cube length and width deviate noticeably from the intended 500 µm dimension (Figure 4A). This was already expected, given the DLP's digital micromirror device (DMD) design and orientation. Taking the position and orientation of the 50 µm square pixels into account, the expected length and width of the printed cubes cross-section lies between the diagonals of 7 or 8 pixels (494.97 µm; 565.68 µm, as explained in Supporting Information). At 50 µm layer height, the chosen parameters produced results closer to the expected value of 8-pixel diagonals compared to 100 µm. When further investigating the printed results for 50 µm layer height and evaluating shape fidelity as the deviation from the expected printed dimension of 565.68 µm, two datasets stand out, yielding the highest shape fidelity. These sets both had a body layer exposure time of 5.5 s and different base layer exposure time factors of 3× and 5×. Between the two different base layer exposure time factors, the 5× base layer exposure time factor showed slightly lower variability (SD = 34.54 µm for length and SD = 26.5 µm for width) and correspondingly lower standard error of the mean (SEM) values (mean length 574.46 µm, SEM = 3.77 µm and mean width 572.79 µm, SEM = 2.9 µm). Under the 5.5 s 3× printing parameters, the mean printed length was 57 446 µm (SD = 34 µm, SEM = 377). More importantly, only the mean printed width (mean 568.41 µm, SD = 4075 µm, SEM 4,47 µm) under these conditions was closest to the expected value. Although the 5× condition produced slightly tighter distributions, the 3× factor provides higher geometric accuracy. Mean dimensions closer to the expected values are prioritized over marginally improved precision around a systematically shifted mean for the parameters used here (full statistical overview provided in the Supporting Information). The one-sample *t*-test confirmed that the mean width did not differ significantly ($p > 0.05$) from the expected value, while showing a significant difference in the mean length compared to the expected ($p < 0.05$; Figure 4A).

The general observable tendency of the printed dimensions to be larger than expected can be attributed to the overexposure. When layers are overexposed, more photons per area are delivered, increasing the probability of photons diffusing out of the intended exposure areas. As a result, they initiate polymerization reactions in surrounding resin, leading to printed features that are larger than intended [43]. Inspection of the printed lengths and widths shows that, regardless of the chosen parameters, all printed lengths differ significantly from the expected 565.68 µm. A potential explanation for this phenomenon may be that the cubes' lengths were measured along the side of the cross section parallel to the long side of the DMA (see Supporting Information). If the slide is slightly nonparallel to the projection plane, one side of the slide is closer to the constrained surface than the other. This problem arose because the parameter optimization was performed using an earlier version of the fixture-carrier system, which did not allow the fixture to pivot freely during the leveling. Consequently, once tilted at an angle α, one side of the printed layer is closer to the constrained surface than the other along the length of the cube. This misalignment would have increased the exposed length by the factor $1/\cos(\alpha)$ compared to an ideally parallel build surface.

Qualitative inspection of the results shows that fewer cubes were printed when the layers were underexposed. With shorter exposure, fewer photons reach the interface between the build surface and the ink preventing sufficient cross-linking to ensure proper adhesion. As result the structures can be printed incorrectly with dimensions smaller than expected, or not at all.

Based on these insights, the printing parameters were set to a 50 µm layer height, 5.5 s body layer exposure time and a 3× base layer exposure time factor. In the cases of 3D printing geometries with drastic overhangs or undercuts, Tartrazine was added and balanced by marginally increasing the body layer exposure time. For geometries with significant overhangs or undercuts, Tartrazine was introduced as a photo absorber. The corresponding body layer exposure time was increased to compensate for the photo absorptive effects of Tartrazine.

2.4 | Capabilities of the Developed System and Process

With the printing parameters optimized and compartmentalization ensured, we next demonstrated parallel 3D printing on SLIPS–DMAs. The process enables 3D bioprinting of geometrically distinct structures in spatially separated hydrophilic spots. Importantly, all structures can be printed in a single step without the need for traversing between compartments. To showcase this capability, we 3D printed an array of 70 structures of 5 different geometries using the developed setup (Figure 4C(A)). The ink consisted of 10% bovine GelMA solubilized in PBS with 0.01% w/v photoabsorber. 3D printing was performed considering the optimized parameters and photoabsorber concentration with a body layer exposure time of 5.75 s and a base layer exposure time

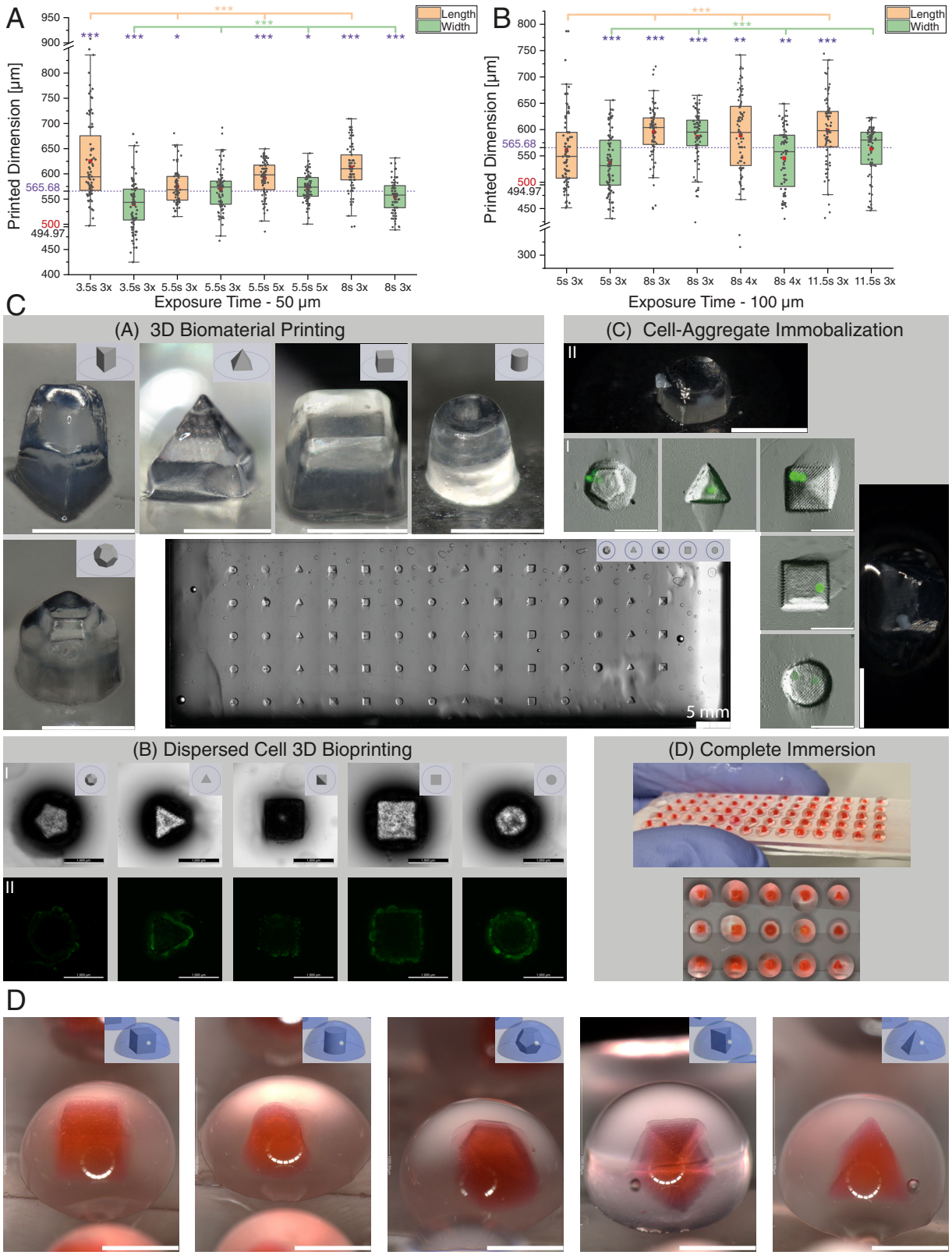

FIGURE 4 | Optimization of printing parameters and demonstration of the developed parallel 3D bioprinting process's capabilities on SLIPS–DMA platforms. (A,B) Comparison of measured versus expected (56 568 µm) dimensions of printed test cubes (0.125 mm^3, 500 µm intended) fabricated using 10% w/v bovine GelMA in PBS 1× with varying base- and body-layer exposure times and layer heights ((A) 50 µm; (B) 100 µm). (C) Demonstration of parallel 3D biomaterial and bioprinting capability using the optimized parameters on SLIPS–DMA. Bright field image of a complete slide immersed in PBS showing an array of 70 simultaneously 3D printed structures, representing five distinct geometries (middle). All of 1 mm characteristic length and height structures were fabricated using 10% GelMA ink containing of 0.25% w/v lithium phenyl-2,4,6-trimethylbenzoylphosphinate (LAP) and 0.01% w/v Tartrazine. Total print time for the full array: 6 min 30 s. (C(A)) Free-standing 3D biomaterial print of five geometries after liquid removal (dodecahedron,

factor of 3×. This resulted in the complete array being fabricated in 6 min 30 s. Out of 80 available hydrophilic spots on the slide, 70 spots fit in the projection screen to be printed (Figure 4C). Compared to existing serialized DLP technology on well plates (e.g. Cellink BionovaX), this parallel process reduces printing time by a factor of 70.

During parameter optimization and surface compatibility testing, arrays of up to 588 structures (14 × 42 cubes) were printed, further highlighting the throughput advantage (see Supporting Figure). Achieving such high spot density required a spot size of only 1 mm^2, which restricted the printable structures to edge lengths of 0.5 mm. These structures could not be fully immersed in droplets formed on the hydrophilic spots. Only when using conical tapered pyramids with edge lengths of six pixel diagonals at the expense of print fidelity, they could be immersed (Figure 2C(B),C(C), Supporting Figure). This limitation arises from the spot size constraint in combination with the pixel resolution of the specific 3D bioprinter used in this study. The parallel printing concept and the DMA platform itself are not restricted by this hardware limitation and can be applied to different SLIPS–DMA layouts using various parallel 3D printing technologies with larger projection areas or higher resolutions. Because both the printer technology and the SLIPS–DMA layout can be freely adjusted, the approach readily extends to larger printable areas, smaller feature sizes, more complex geometries and to SLIPS–DMAs with either smaller or larger hydrophilic spots and their corresponding compartmentalizable droplet volumes. This flexibility enables tailored ultrahigh-throughput screenings with tunable ratios between printed structure volume and the surrounding liquid environment. Utilizing the current lumen X+ Bioprinter in combination with the 10% w/v GelMA formulation, the smallest reliably printable free standing structures were pyramidal features with a characteristic length of five pixel diagonals (354 μm). This printer-resin combination limited feature size is consistent with the relatively low polymer content and high water fraction of GelMA combined with the 50 μm pixel size of the LumenX+ Bioprinter.

Parallel 3D printing on SLIPS–DMAs further enables high-throughput 3D cell culture together with multiplexed screening of interactions between cells, hydrogels, and solubilized drugs in the surrounding medium. To practically demonstrate the capabilities of the developed process and system, we printed the same model of 5 different geometries in a 70 structure array with dispersed HEK-293 cells at a concentration of 10^6 cells/ml. This approach minimized cell-induced light scattering that would otherwise hinder printability. The structures were printed successfully and the incorporated cells could be stained with calcein, Hoechst and propidium iodide (PI) solubilized in the surrounding liquid droplet. Cells remained viable as confirmed by calcein staining, with minimal cell death indicated by PI staining (Supporting Information). The DLP technology is not expected to be phototoxic, as its illumination system operates at a safe 405 nm wavelength, thereby ensuring cell viability. Successful staining confirmed that the resulting porosity of the cross-linked 10% GelMA ink at the optimized printing parameters allows diffusion of dyes of varying molecular weight (452.55 Da (Hoechst 33342), 668.40 Da (Propidium Iodide), 994.86 DA (Calcein-AM)). This suggests that cellular nutrients or metabolic byproducts with substantially lower molecular weights (180.16 Da (Glucose), amino acids 89.09 Da (Alanine), and 89.07 Da (Lactate)) may be able to diffuse between hydrogel structure and solution for nutrients and waste exchange between cells in the hydrogel structure and the medium around it. Additionally, the staining confirmed that cells mixed into the hydrogel ink, even when partially exposed to the SLIPS surface during printing, remain viable. This observation was expected, since cell–laden hydrogel structures form only within the PFPE-free hydrophilic spots. Viability staining performed after 48 h of incubation also demonstrated that the PFPE lubricant remains stably confined within the nanoporous superhydrophobic matrix, while the aqueous droplets containing culture medium remain strictly pinned to the hydrophilic compartments. Because the 3D-printed hydrogel structures are positioned entirely within the hydrophilic spot, the surrounding droplet acts as an aqueous layer separating the GelMA construct from the PFPE-infused background. Although this aqueous phase may contact the thin PFPE surface layer present on the nanostructured SLIPS background, the 3D hydrogel structure when cultured is not. Since PFPE oils are effectively insoluble in water, this spatial configuration prevents any meaningful PFPE transfer into the hydrogel. With a 1 mm construct inside a 2.8 mm hydrophilic spot, the printed structures maintain a minimum aqueous separation of 0.7 mm from the water SLIPS interface on the slide, ensuring complete immersion in medium and isolation from the lubricant phase.

With cell viability confirmed, we demonstrate immobilization of cell aggregates (Figure 4C(C)). Printed hydrogel structures are used to trap HEK-293 spheroids serving both as a scaffold

triangular prism, pyramid, cube, and cylinder). (C(B)) 3D bioprinting with dispersed cells: Same cad models printed with HEK-293 cells (10^6 cells/mL) mixed with GelMA ink during preprocesing. Bright field image (*I*) of printed structures and postprinting viability analysis of cell laden structures via Calcein staining (*II*). (C(C)) 3D bioprinting with preformed HEK-293 cell-spheroids embedded in the 3D printed hydrogel structure. Overlay of brightfield and Calcein fluorescence images *(I)* showing immobilized spheroids within 3D printed scaffold structure. Close up images (II) showing free-standing 3D bioprinted structures containing fully embedded spheroids and partially exposed spheroids. (C(D)) Overview of the final state of the 3D printed array on the SLIPS–DMA for HTS. Showing droplet formation around partially spot-covering constructs, printed with shape fidelity optimized printing parameters, enabling wall-less liquid compartmentalization for downstream HTS. (D) lose-up images of individual, red-dyed structures fully immersed in compartmentalized PBS 1X droplets (arrays of free-standing structures in Supporting Information). For all images the corresponding 3D CAD models are shown in each upper right corner. Scale bars, 1 mm unless stated otherwise. One-way ANOVA showed significant effects of exposure conditions on printed length (orange) and width (green) ($p < 0.0001$, ***, **, * indicate $p < 0.001$, 0.01, 0.05). Differences from the expected value (565.68 μm) were assessed by independent-samples *t*-tests (purple) ($p \leq 0.05$). Box plots show the median (line), interquartile range (IQR) box (25–75%), whiskers (1.5 × IQR), outliers (points) and mean (red square). Sample sizes were $n = 83$–84 (50 μm) and $n = 79$–84 (100 μm). Individual data points are overlaid to display measurement spread. Overview and further details are depicted in Supporting Information.

and fixation element. Because the 3D structure can be tailored to partially cover a hydrophilic spot, liquid droplets can still form around the structures (Figure 4C(D),D). This demonstrates the capability of the process to either fix cell-aggregates or dispersed cells in a straightforward manner, while maintaining compatibility with multiplexed screenings on the platform.

The essential requirement for 3D printing on a patterned, biomaterial-repellent surface was met by introducing PFPE into the nanoporous surface to create a SLIPS–DMA. Consequently, a reduction of the advancing contact angle was introduced to the hydrophobic background of the pattern on the SLIPS–DMA (Figure 2F(A), θ_a for SH; Figure 2F(D), θ_a for SLIPS, respectively). We experimentally validated that the advancing contact angle of the SLIPS is sufficient to compartmentalize liquid volumes large enough for complete immersion of the printed structures. For this test, we used the previously printed array of 70 structures of five different geometries made from 10% GelMA ink, each with an edge length of 1 mm, only partially covering circular hydrophilic spots of 2.8 mm. During postprocessing, PBS 1X solution was dispensed automatically using a Certus Pro Flex liquid dispenser (Figure 3G). On the SLIPS–DMA, the nanoporous, PFPE-treated background provides a sufficiently high advancing contact angle to define the maximum droplet volume required for complete immersion. Combined with the large contrast in wettability, this allows the liquid to be retained in a stable droplet around the structures (Figure 4D).

3 | Conclusion

In conclusion, this work bridges the gap between parallelized HTS and the fabrication of 3D tissue substitutes, overcoming the long-standing trade-offs between physiological relevance and fabrication speed. We establish a generalizable approach for truly parallel 3D bioprinting that is compatible with miniaturized, wall-less liquid compartmentalization platforms, paving the way for scalable high-throughput 3D biofabrication. By integrating DLP stereolithography with a SLIPS–DMA, we demonstrate the first truly parallel 3D bioprinting process on a liquid compartmentalization platform. Previous parallel fabrication approaches, such as mold-based replication or lost-form casting, allow rapid structure production, once a mold is available, but involve time-consuming mold manufacturing and inherently restrict flexibility in geometry and array design [27]. Attempts to adapt natively parallel DLP technology had to be serialized to overcome the constraints imposed by physical walls required for compartmentalization [7, 44]. The main drawback of common serial additive manufacturing approaches for 3D biofabrication on HTS platforms is that printing time scales directly with the number of structures in the array. In contrast, our approach enables arrays of freely designed structures in high densities to be produced in parallel directly on the compartmentalization platform. For instance, an array consisting of 70 3D structures was printed in 6.5 min, reducing print time by a factor of 70 compared with serial methods (>7 h). Even larger arrays containing up to 588 structures (Figure 2C, and Supporting Information) were fabricated in under 3.5 min due to their reduced height (compared to >34 h in serial). Furthermore, the ability to generate libraries of controlled 3D geometries at this scale enables addressing experimental questions that cannot be answered with conventional spheroids used as tissue substitutes. The introduced system allows screening of shape-dependent biological effects where geometry is a key regulator of cell fate decisions and diffusion-limited drug responses. Precise control over parameters such as curvature, aspect ratio and surface-to-volume ratio in the design process underlines this capability. In addition, the high geometric fidelity and reproducibility of these sub-millimeter 3D constructs enable downstream computational analyses such as finite-element modeling (FEM). FEM can be used to quantify predicted stress, strain, or diffusion fields and relate them to experimentally observed mechanobiological responses under applied mechanical or biochemical stimuli. Comparable screening is currently impossible in high-throughput formats due to the difficulty of producing diverse 3D structures at scale.

Looking forward, the number of individual 3D tissue substitutes on a larger area can be scaled up by using masked stereolithography (mSLA) as another projection stereolithography system. Since our method only requires a uniform projected dynamic photomask, the developed workflow remains unchanged even when moving to larger or smaller projection fields. Likewise, the SLIPS–DMA can be fabricated on glass substrates of any matching size or resolution. Further down the line, ongoing miniaturization efforts combined with advancements in projection-based 3D printing technologies will enable denser arrays of 3D printed hydrogel structures with smaller feature sizes, to be printed more reliably and with greater detail, further expanding screening capacity. The drastic reduction in fabrication time also opens new possibilities for HTS experiments using time-sensitive primary cells that previously could not be processed within practical time frames in arrays of these sizes sequentially.

Future time improvements can be made by introducing continuous liquid interface production (CLIP) [45] technology, though the primary advance in the form of an array-size-fold reduction in fabrication time, arises from the transition from sequential to parallel fabrication. The developed system and process establish a high-throughput system-on-a-chip platform for 3D cell culture and straightforward immobilization of cells, whether as single cells, dispersed cells, or multicellular aggregates. This method supports compartmentalized multiplexed screening of interactions at multiple levels: between cells and hydrogels, between cells and surrounding media or drugs and between hydrogels and solubilized compounds. As this work establishes the technological basis for parallel 3D bioprinting on SLIPS–DMAs, integrating standardized assays with the unique open droplet 3D culture environment presents valuable opportunities to develop tailored solutions, that fully exploit the platform's potential.

Overall, the presented process redefines throughput limits in 3D bioprinting and establishes a foundation for scalable, miniaturized 3D biofabrication compatible with automated, multiplexed assays. Its compatibility with complex biomaterial inks and live-cell printing, while maintaining compartmentalization, unlocks new experimental possibilities for tissue engineering and drug discovery. Further developments in truly parallel 3D bioprinting will help providing a pathway to transform 3D bioprinting from a sequential prototyping method into a reliably usable tool for high-throughput applications capable of capturing biological complexity at scale.

4 | Methods

4.1 | Engineering

The developed fixture was designed and manufactured in the rapid prototyping process using Autodesk inventor as well as Autodesk Fusion 360 for the CAD design and Chitubox as slicer. The different version of the fixture and the carrier system were 3D printed in the mSLA process (Elegoo, Saturn S). The 3D printed parts were manufactured from epoxy acrylate resin (Siraya Tech, Blu-Tough Resin). Off-the-shelf parts include DDIN7991/ISO10642 screws, DIN934 nuts, ISO 3601 O-rings and DIN 2098 compression springs for the fixture. LME linear bearings and Din EN 10305-1 precision pipes for the linear guiding system of the carrier, as well as DIN 975 threaded rods and DIN 934 nuts to attach the linear guidance system to the commercial bioprinter.

4.2 | DMA

Patterned DMAs and subsequently SLIPS–DMAs were fabricated following the patented protocol [21]. Borofloat glass slides (75.6 × 25 × 1 mm) were used as substrates (Schott, Nexterion). According to the manufacturer, the slides were cleanroom-cleaned to remove physical contaminants, but not plasma- or UV-cleaned. The cleaning process involved an ultrasonic cleaning line with multiple rinsing and drying steps using infrared radiation and proprietary cleaning agents for optical glass. This treatment resulted in a static contact angle of $\theta_m = 16.6°$, consistent with values reported for clean glass surfaces considering that the specific cleaning solution is unknown [46–48]. The slides were activated by treating them with 184.9 and 253.7 nm light (30 mW/cm^2,10 min, Jetlight Co. Inc., UVO Cleaner 42-220).

For the coating solution, 250 mg of silica nanoparticles (Evonik, Aerosil 200) were mixed with 30 mL ethanol and sonicated for 30 min. Next, 330 µL of vinyl trimethoxysilane (Sigma-Aldrich) were added along with 200 µL concentrated hydrochloric acid (HCl; 37%, ThermoFischer Scientific). The mixture was sonicated an additional 60 min and then aged for 24 h before use.

The coating solution (500 µL) was deposited onto the activated slides by spin-coating (SPS Europe) for 15 s at 1500 rpm, repeated 5 times per slide and cured at 200°C for 1 h. After baking, the slides were wetted with a 10 vol% solution of 1H,1H,2H,2H-perfluorodecanethiol (PFDT; GenoSynth GmbH) in acetone. The patterned modification was achieved in a photolithographical process by localized UV-C exposure (265nm, Hönle, UVACUBE 2000) through a photomask (Rose Fotomasken) for 90 s. Slide and photomask were then separated and subsequently rinsed with acetone and dried with compressed air. Hydrophilic spot modification was performed by pipetting 500 µL of a 10 vol% 2-mercaptoethanol solution (1:1 mixture of water and ethanol) onto the slide and placing a quartz glass plate on top for uniform coverage. This procedure resulted DMAs with in patterns like 80 circular spots (15 columns × 6 rows) with a spot-diameter of 2828 µm, a center-to-center pitch of 4.5 mm and a maximum aqueous solution compartmentalization capacity of 15 µL per spot. This layout offers an inherent geometric safety margin, that prevents coalescence under standard gentle handling of the open droplet platform.

4.3 | SLIPS–DMA

The combination of a patterned surface of locally different wettabilities and hydrogel repellency was achieved following previously established protocols [28, 29]. After completion of the patterning process, the hydrophilic spots were covered with water droplets by parallel discontinuous dewetting to prevent oil immersion there. For this, the whole DMA was briefly submerged in deionized water and retrieved after 5 s.

The prepared slide was then placed in a small container (e.g., a 4-well plate) and 10 mL of perfluoropolyether oil (PFPE; Krytox, GPL103) were gently poured over the surface until the droplets were completely covered. The slide was left immersed for at least 30 min to ensure sufficient infusion of the nanoporous coating with oil. After removal, the slide was left in a partially open 50 mL Falcon tube (ThermoFischer Scientific) to allow excess PFPE oil to drip off, while preventing desiccation of the hydrophilic spots. To accelerate the preparation for printing, the droplets on the spots were evaporated by exposure to dry air or by mild heating on a hot plate, yielding the SLIPS–DMA substrates. All steps in this procedure can be performed on multiple DMAs simultaneously and scale directly with the volume of the water and oil baths, enabling efficient parallel preparation of large batches of SLIPS–DMA slides. After evaporation of the surface droplets, the prepared SLIPS–DMAs can be stored long term in sealed 50 mL Falcon tubes (ThermoFischer Scientific) without loss of function.

5 | Surface Characterization, Water Contact Angle

5.1 | Surface Preparation

Completely superhydrophobic and subsequently uniform SLIPS slides (without hydrophilic patterning) were prepared following the patented protocol for patterned DMA fabrication up to the baking step after spin-coating [21]. A spin coated slide was wetted with a 10 vol% solution of PFDT (GenoSynth GmbH) in acetone. The photolithographical process was performed without a photomask UV-C exposure (265 nm, Hönle UVACUBE 2000) through a quartz glass pane for 90 s. Slide and glass pane were then separated and subsequently rinsed with acetone and dried with compressed air.

After drying, the prepared slide was then placed in a small container (e.g., a 4-well plate) and 10 mL of perfluoropolyether oil (PFPE; Krytox, GPL103) were gently poured over the surface. The slide was left immersed for at least 30 min to ensure sufficient infusion of the nanoporous coating with oil.

The 3D printing process was emulated by exposing slides with different surface treatments, to the 10% w/v GelMA biomaterial ink for 10 min, followed by washing in PBS (1X, Sigma-Aldrich) at 45°C for 20 min.

5.1.1 | Statistical Analysis for Static Contact Angle Measurements

Contact angles were measured using an automatic drop shape analyzer (DSA25S, Krüss). The static WCA was determined from a 3.5 µL droplet to minimize gravitational deformation. To minimize measurement error, the mean static WCA (θ_m) was calculated as the average between the right (θ_r) and left (θ_l) WCA of the droplet. Similarly, the static contact angle of the 10% GelMA PBS solution (θ_{st}) was derived as average of its left and right contact angle. The DSA platform was levelled before each measurement using a water level, but small differences between sides may result from persisting slight sample tilt. Statistical significance between the mean static WCAs was determined by paired sample *t*-tests with a significance threshold of $p \leq 0.05$. Results are reported as highly significant ($p < 0.001$,***), very significant ($p < 0.01$, **) and significant ($p < 0.05$,*). Values above that level are indicative of statistical insignificance.

Contact angle data was visualized using bar charts for straightforward comparison of the sample mean to facilitate visual comparison for statistical differences. The bar height represents the sample mean and a horizontal line within each bar marks the median. Error bars indicate variability, defined as +1.5 times the SEM. Sample sizes were $n = 15$ for untreated SH and SLIPS surfaces, $n = 5$ for postprinting and 24 h washing conditions, and $n = 4$ for hydrophilic glass. Individual data points are overlaid to display measurement spread. A summary of the *t*-tests are presented in the Supporting Information.

The advancing WCA (θ_a) was measured primarily with the tilting plate method (θ_{a1}) and validated using the syringe method (θ_{a2}) in either needle-in or needle-on configurations. Furthermore, the tilting plate method was used to determine the WCA hysteresis as well as the roll-off angle. Each measurement was performed in five independent replicates and for the syringe method, a minimum of five locations were analyzed with a minimum of three repetitions per site, with the mean value reported for each measurement method (θ_{a1}, θ_{a2})

As the tilting plate method resulted in very narrow WCA hysteresis for surfaces where the contact line was mobile (SH and SLIPS), the receding WCA provided limited additional information. Only the advancing WCA was therefore reported, as it defines the maximum compartmentalizable droplet volume before roll-off. For the tilting plate method, 10 µL droplets were used to guarantee sufficient gravitational influence to initiate movement and avoid pinning. The advancing WCA (θ_a) was determined as the maximum WCA on the downhill side of the droplet during its transition from a static state to the initiation of macroscopic movement. After initial droplet deposition, the slide was tilted with 10°/s until 90° tilt, or until the droplet moved macroscopically.

In cases where the angle reached its maximum just prior to visible movement (indicating strong pinning), the value from the last static frame was selected. For measurements where the angle continued to increase and peaked precisely at the onset of movement (suggesting a smoother transition or less dominant pinning), the angle from the first frame showing motion was utilized. Small differences (e.g., < 0.5°) between adjacent frames at this transition point were attributed to measurement noise or the discrete nature of frame capture. The corresponding roll-off angle was consistently recorded as the tilt angle at which the droplet's contact line was first observed to move.

For the syringe method an initial droplet of approximately 3.5 µL was formed and depending on the configuration either lowered onto the substrate or positioned, with the needle in the center of the sphere and then a liquid of 15 µL was dosed at a flow rate of 0.5 µL/s. The needle-in configuration was primarily used, in which an initial droplet (3.5 µL) was first deposited on the surface where a needle was subsequently inserted into its center in close proximity to the substrate to dispense additional liquid (15 µL, 0.5 µL/s). On superhydrophobic surfaces the droplet tended to adhere to the less hydrophobic needle, forming a nonrepresentative WCA. Therefore, the needle-on configuration was additionally employed, where liquid was dispensed directly from the needle onto the surface (0.5 µL/s). In this configuration, the needle served as the initial point of contact to prevent climbing of the droplet on the needle rather than moving along the substrate-droplet-air interface. In both cases, the advancing WCA was identified as the maximum stable angle prior to visible contact line motion signifying the droplet breaking free from the pinned state.

Generally, the inbuilt software of DSA25S (Krüss ADVANCE) was used to determine the contact angles in all cases. The software then applies a mathematical algorithm (Tangent-1 method) to fit an ellipse to the detected droplet profile, or a truncated ellipse when only part of the droplet profile is visible. Due to unreliability issues with the automatic baseline detection algorithm, the manual baseline option was selected.

A droplet volume of 3.5 µL (below 5 µL) was used for all static contact angle measurements to minimize droplet deformation caused by gravitational force, as commonly reported [49, 50]. For the tilting plate, larger droplets (10 µL) were required to generate sufficient gravitational force to overcome surface adhesion and initiate droplet movement on GelMA-exposed SH slides. To ensure comparability, all surfaces were tested using 10 µL droplets to determine the advancing contact angle. Further discussion of volume-dependent deformation effects on the SH surface is provided in the Supporting Information.

Due to the tilting plate method yielding very narrow WCA hysteresis for the surfaces where the contact line could move (SH & SLIPS), the values measured for the receding WCA were not reported.

Ultralow contact angles in the range of superhydrophilicity ($\theta <$ 10°) were not quantifiable with the current DSA. This limitation arose because the thin liquid layer formed at these angles did not provide sufficient contrast for reliable goniometric fitting against the substrate, given the inherent constraints of the DSA's illumination and camera system.

Additionally, the advancing contact angle on SH slides exposed to GelMA ink could not be determined using the tilting plate

method, as the water droplets remained completely pinned up to a tilt angle of $\alpha = 90$. During measurements with the syringe method, the droplet overcame the pinned state through the applied external pressure generating reportable results (θ_{a2}).

5.1.2 | Statistical Analysis for Dynamic Contact Angle Measurements

Dynamic contact angle measurement data was presented using bar charts representing the mean (bar height) with the median indicated as a horizontal line; error bar shows +1.5× SEM. Individual data points are overlaid to display measurement variability.

6 | Bio Ink

For the initial test prints during the development of the fixture system making the DMA compatible to the DLP bioprinter, PEGDA ink (Cellink [51], PEGDA PhotoInk,) was used which is preformulated with 50% PEGDA (700 MW) with 0.5% lithium phenyl-2,4,6-trimethylbenzoylphosphinate (LAP).

6.1 | Biomaterial Ink Preparation

Methacryloyl-modified porcine gelatin (GelMA; Sigma-Aldrich, Type A, ∼300 g bloom) was synthesized as previously described [52]. Briefly, 1 g of porcine gelatin powder (1 eq., 0.259 mmol lysine residues) was solubilized in 10 mL in 0.25 M carbonate-bicarbonate (CB) buffer pH 9 at 50°C under constant magnetic stirring. Next, the pH of the solution was adjusted to 9.4 with sodium hydroxide (Sigma-Aldrich) and 310 µL of methacrylic anhydride (8 eq., Sigma-Aldrich) were added dropwise under constant magnetic stirring at 50°C. After 2.5 h, the pH of the mixture was neutralized to 7.4 with HCl 1 M and dialyzed against DI water for 3 days with 3 water changes per day. The obtained product was lyophilized and stored at −20°C protected from light until further use.

The degree of modification (0.437 mmol methacryloyl/g of dry GelMA) was calculated by H-NMR in deuterium oxide (1 mg/mL 2,2,3,3-D4, D, 98%, Sigma-Aldrich) sodium-3-trimethylsilylpropionate (TMSP; Sigma-Aldrich) as internal standard following a previously reported method [53] (spectrum and equation provided in the Supporting Information).

PBS 1X, was used as the solvent for creation of the photocurable biomaterial ink. The hydrogel ink was prepared at a concentration of 10% w/v GelMA. As photoinitiator LAP (Sigma-Aldrich) was used at a concentration of 0.25% w/v. For the bioprinting experiments where biomaterial ink was combined with cells prior to printing, sterile Dulbecco´s Phosphate Buffered Saline 1× (DPBS; ThermoFisher Scientific) was used, and the LAP stock solution was filtered through a 0.20 µm syringe filter. Tartrazine (ThermoFischer Scientific) was added to the ink at a concentration of 0,01% w/v.

An additional rheological characterization of the biomaterial ink used in this study is provided in the Supporting Information.

6.2 | 2D Cell Culture

HEK-293 human embryonic kidney cells (CRL-1573, American Type Culture Collection) were cultured in Dulbecco's modified Eagle's medium (DMEM; ThermoFischer Scientific) supplemented with 10% fetal bovine serum (FBS; ThermoFischer Scientific) and 1% penicillin–streptomycin (ThermoFischer Scientific). Cells were passaged every 2–3 days and maintained in standard cell culture incubator at 37°C and 5% CO_2.

6.3 | Spheroid Fabrication

HEK-293 (CRL-1573, American Type Culture Collection) cell spheroids were fabricated using the hanging drop method [54] on a DMA with 672 hydrophilic spots. To ensure sterility, the DMA was immersed in ethanol and air-dried under a clean bench to dry. Each spot on the slide was coated with 50 nL of a 50% Anti-Adherence Rinsing Solution (Stemcell Technologies) in water using an I.DOT One dispenser (Dispendix). After drying, 200 nL of a cell suspension containing 2,5 × 10^6 cells per mL (corresponding to 500 cells per spot) were dispensed onto the DMA. The slide was then inverted on a custom-designed 3D-printed holder and incubated in a petri dish containing a humidifying pad in DPBS 1X (ThermoFisher Scientific) for 48h at 37°C and 5% CO_2. After incubation, the spheroids were collected using a wide-opening pipette tip and gently mixed with the biomaterial ink for downstream 3D bioprinting applications

6.4 | Bioink Preparation

Adherent cells had to be detached, suspension cells had to be concentrated and resuspended and cell aggregates had to be cultured and biofabricated in advance. For printing with dispersed cells, they were washed with sterile DPBS 1X (ThermoFischer Scientific) and detached using 0.25% trypsin–ethylenediaminetetraacetic acid (EDTA) (ThermoFischer Scientific) at 80% confluency. After neutralization with complete medium, the cell suspension was collected and centrifuged at 1200 rpm for 3 min. The pellet was resuspended in fresh medium. Cell concentration and viability were determined using an automated cell counter (ThermoFischer Scientific, Countess II) with trypan blue (ThermoFischer Scientific). A cell suspension with a final concentration of 1 × 10^6 cells per mL was prepared and mixed with the biomaterial ink by gentle pipette resuspension.

6.5 | 3D Cell Culture

3D bioprinted tissue substitutes, fabricated with dispersed cells or cell spheroids were cultured on the SLIPS–DMA platform. The slide holding the cell laden 3D structures was incubated in a petri dish immersed in DMEM (ThermoFischer Scientific) supplemented with 10% FBS (ThermoFischer Scientific) and 1%

penicillin–streptomycin (ThermoFischer Scientific) in standard cell culture incubator for 48 h at 37°C and 5% CO_2.

6.6 | Cell Stainings

3D bioprinted hydrogel constructs on the DMA were stained using an I.DOT One dispenser (Dispendix GmbH). A total of 3 µL of staining solution was dispensed per hydrophilic spot, containing Calcein-AM (1:2000), PI (1:1000), and Hoechst (1:1000) in DPBS. Calcein-AM, Hoechst 33342 and PI were purchased from Invitrogen (Thermo Fisher Scientific). The tissue substitutes were then incubated for 30 min at 37°C, 5% CO_2, followed by fluorescence imaging (Leica Microsystems, Thunder 3D Imager). Imaging of the 3D bioprinted structures was performed after staining and incubation for 30 min with the slide and structures fully immersed in PBS in 4-well plate in an inverted microscope (Keyence, BZ-X800)

Further experimental procedures related to parallel 3D bioprinting, extended SLIPS–DMA 3D cell culture, and qualitative doxorubicin-based cytotoxicity profiling using KIT-8 colorimetric staining and Grid Screener-based automated readout [55] are provided in the Supporting Information.

7 | Parameter Optimization

588 cubical 0.125 mm^3 structures (0.5 mm edge length, 14 × 42) were 3D printed on a DMA containing 672 (14 × 48) square 1 mm^2 spots. Because the Lumen X+ printing screen (64 × 40 mm) is smaller than the patterned DMA area (756 × 25 mm). 3D printing was performed in the near-UV light spectrum (405 nm) at a 50% power level of the illumination system, corresponding to a 20 mW/cm^2 intensity, as specified by Cellink and validated using an optical power and energy meter (Thorlabs, PM100D). Two of the eight printed rows across all 42 columns of cubes, located in the middle of the slide, were analyzed. These two central rows were selected because print success was highest in this region, independent of printing parameters. If a considerable number of cubes were missing, the two rows containing the highest number of complete structures were selected.

The base layer exposure time is defined as a multiple of the body layer exposure time. For example, with a body layer exposure time of 5.5 s, factors of 3× and 5× result in base layer exposure times of 16.5 and 27.5 s, respectively.

7.1 | Statistical Analysis of the Printing Parameter Optimization

The experimental design for the parameter optimization was statistically validated through four separate one-way ANOVA analyses for the printed lengths and widths for both layer heights. A p-value of <0.0001 was determined for the printed length and width at 50 µm layer height. These results confirmed that the selected printing parameters were effective, causing a statistically significant change in the mean dimensions of the printed parts. Sample sizes for each condition were n = 83–84 for 50 µm and n = 79–84 for 100 µm layer heights, depending on printing success.

Statistical significance between the mean measured length or width and the expected dimension of eight DMD pixel diagonals (565.68 µm) was evaluated using independent samples t-tests. A significance level of $p \leq 0.05$ was used for all comparisons. In this context, a highly significant result is indicated by $p < 0.001$ (***), a very significant result by $p < 0.01$ (**) and a significant result by $p < 0.05$ (*). Values above this threshold were considered statistically insignificant (specific results of the ANOVA & t-tests are presented in the Supporting Information).

The length of the error bar was determined by an error bar coefficient (1.5). Box plots were used to visualize the datasets generated during parameter optimization, highlighting data spread and identifying outliers. Each box represents the interquartile range (IQR) between the 25th (Q1) and 75th (Q3) percentiles. Whiskers were defined using Tukey's rule, extending to the most extreme data points within 1.5 × IQR of the box limits (upper whisker = Q3 + 1.5 × IQR; lower whisker = Q1 − 1.5 × IQR). Data points beyond these limits are shown as individual outliers. The median is indicated by a horizontal line within the box, and the mean by a cube marker.

8 | Printing Process

Prior to printing the patterned SLIPS–DMA slides were mounted into the custom carrier fixture. In the case of bioprinting, the SLIPS–DMA can be sterilized through five successive submersions in 70% ethanol. If necessary, the clamping force could be adjusted by rotating the side-accessible screws. The fixture holding the SLIPS–DMA was placed in the carrier with the locking screws left untightened. The printer initiates the leveling process by lowering the z-axis with the carrier attached. During leveling, the SLIPS–DMA was pressed against the constrained surface to ensure parallelism between build surface and projection plane. Once alignment is achieved, the vacuum system was activated to pull the slide against the fixture. The fixture was then constrained to linear motion along the z-axis during printing, by tightening the four bolts (Figure 3D).

After leveling, the z-axis assembly is lifted from the constrained surface to clear the vat and allow the prepared biomaterial or bioink to be dispensed. In the case PFPE oil residue could occurring after of contact with the constrained surface, it was removed by wiping the vat with a fiber-less wipe (KIMTECH Science, precision wipes). The prepared ink was dispensed in the vat after preheating to 45°C, which was verified using an IR thermometer on the constrained surface. A continuous bead of 1.5 mL was dispensed along the diameter of the vat. Printing was performed at 405 nm (20 mW/cm^2) using optimized base and body layer exposure times, as determined by parameter screening. After the printing process finished, the carrier-fixture assembly moved away from the vat. The locking screws attaching the fixture to the carrier were opened to remove the fixture from the carrier. The fixture allows reversal of the adhesion mechanism of the slide to the fixture by turning off the vacuum. Next, the two halves of the fixture were pulled apart and the SLIPS–DMA was removed from the fixture. After removal the slide with the printed

structures on them was washed to remove the un-cross-linked ink for 20 min. If a thermoreversible gelating biomaterial ink is used, the washing step had to be performed at a temperature above the point of gelation, but below the degradation temperature of any protein components. In the case of the bovine 10% w/v GelMA ink the washing solution (PBS 1X, Sigma-Aldrich) was preheated to 45°C, to prevent thermoreversible gelation. Washing efficiency is enhanced by introducing flow to the liquid, for example via magnetic stirring. This facilitates removal of residual ink and ensures clean structures

9 | Compartmentalization Experiments

The transparency of the hydrogel after photoabsorber removal during the washing step, in combined with reflections at the liquid–gas interface, made imaging of the immersed structures in the droplets challenging. To enhance visibility prior to immersion in PBS (1X, Sigma-Aldrich), the 3D printed hydrogel structures were stained by dipping the complete slide in a water-dye solution (Ateco, 120 Super Red). After 20 min incubation, the slide with the structures was removed and the excess dye droplets formed by discontinuous dewetting were aspirated. New droplets of clear PBS were subsequently dispensed using an automated liquid dispenser (Gyger, CERTUS FLEX) to show the printed geometries within spatially separated droplets (Figure 4D).

Storage of the printed structures on the SLIPS–DMA platform was performed either in closed containers with the slides fully immersed or in a humidity-controlled environment to prevent drying out.

Photographs documenting the printed structure's shape were captured after liquid removal or with the prints fully submerged in PBS using a tiltable digital microscope (Keyence, VHX 7000). Incomplete rehydration after liquids removal around the structures could result in shrinking toward the gel-substrate interface and a tapered appearance.

During imaging of structures immersed in compartmentalized droplets, a lens effect originating from the droplet meniscus caused optical distortion of the structures within.

Additional validation experiments confirming long-term droplet compartmentalization and evaporation stability on the SLIPS–DMA platform are provided in the Supporting Information.

10 | Statistical Analysis

Measured values have two decimals, but calculated metrics contain additional decimals due to division. Main-text values are rounded to two decimals. All statistical analysis was performed using Origin Pro 2023 (Academic). Data presentation was performed in Origin and finalized in Adobe Illustrator

11 | Writing & Text

Wording and spelling were reviewed using large language models, including ChatGPT GPT5 and Gemini 2.5 flash.

12 | Visualization

Renderings were created using Autodesk Inventor. Figures were created in Adobe Illustrator. Graphs were created in Origin 2023 and transferred into Adobe Illustrator.

Acknowledgements

The authors acknowledge funding from the Deutsche Forschungsgemeinschaft (DFG, German Research Foundation) through the Excellence Cluster "3D Matter Made to Order" (EXC 2082/1-390761711 & 2082/2 – 390761711), the Carl Zeiss Foundation through the "Carl-Zeiss-Foundation-Focus@HEiKA," and the German Academic Exchange Service (DAAD).

Open access funding enabled and organized by Projekt DEAL.

Conflicts of Interest

The authors declare no conflicts of interest.

Data Availability Statement

The data that support the findings of this study are openly available in [KITopen] at [https://doi.org/10.35097/vd0jd35ttt8dkrg3], reference number [1000187212].

References

1. P. Szymanski, M. Markowicz, and E. Mikiciuk-Olasik, "Adaptation of High-Throughput Screening in Drug Discovery—Toxicological Screening Tests," *International Journal of Molecular Sciences* 13 (2012): 427–452, https://doi.org/10.3390/ijms13010427.

2. D. A. Pereira and J. A. Williams, "Origin and Evolution of High Throughput Screening," *British Journal of Pharmacology* 152 (2007): 53–61, https://doi.org/10.1038/sj.bjp.0707373.

3. R. P. Hertzberg and A. J. Pope, "High-Throughput Screening: New Technology for the 21st Century," *Current Opinion in Chemical Biology* 4 (2000): 445–451, https://doi.org/10.1016/s1367-5931(00)00110-1.

4. A. Mazzocchi, S. Soker, and A. Skardal, "3D Bioprinting for High-Throughput Screening: Drug Screening, Disease Modeling, and Precision Medicine Applications," *Applied Physics Reviews* 6 (2019): 011302, https://doi.org/10.1063/1.5056188.

5. S. Breslin and L. O'Driscoll, "Three-Dimensional Cell Culture: The Missing Link in Drug Discovery," *Drug Discovery Today* 18 (2013): 240–249, https://doi.org/10.1016/j.drudis.2012.10.003.

6. L. A. Kunz-Schughart, J. P. Freyer, F. Hofstaedter, and R. Ebner, "The Use of 3D Cultures for High-Throughput Screening: The Multicellular Spheroid Model," *SLAS Discovery* 9 (2004): 273–285, https://doi.org/10.1177/1087057104265040.

7. H. H. Hwang, S. You, X. Ma, et al., "High Throughput Direct 3D Bioprinting in Multiwell Plates," *Biofabrication* 13 (2021): 2, https://doi.org/10.1088/1758-5090/ab89ca.

8. M. Engel, L. Belfiore, B. Aghaei, and M. Sutija, "Enabling High Throughput Drug Discovery in 3D Cell Cultures through a Novel Bioprinting Workflow," *SLAS Technology* 27 (2022): 32–38, https://doi.org/10.1016/j.slast.2021.10.002.

9. N. Imani Farahani, K. K. L. Wong, G. Allen, et al., "High-Throughput Bioprinting to Produce Micropatterned Neuroepithelial Tissues and Model TSC2-Deficient Brain Malformations," *Cell Reports Methods* 5 (2025): 101177, https://doi.org/10.1016/j.crmeth.2025.101177.

10. R. Dai, W. Chen, Y. Chen, et al., "3D Bioprinting Platform Development for High-Throughput Cancer Organoid Models Construction and

Drug Evaluation," *Biofabrication* 16 (2024): 3, https://doi.org/10.1088/1758-5090/ad51a6.

11. M. de Villiers, A. F. Kotze, and L. H. du Plessis, "Pneumatic Extrusion Bioprinting-Based High Throughput Fabrication of a Melanoma 3D Cell Culture Model for Anti-Cancer Drug Screening," *Biomedical Materials* 19 (2024), https://doi.org/10.1088/1748-605X/ad651f.

12. L. M. Mayr and D. Bojanic, "Novel Trends in High-Throughput Screening," *Current Opinion in Pharmacology* 9 (2009): 580–588, https://doi.org/10.1016/j.coph.2009.08.004.

13. R. Bongiovanni and A. Vitale, *High Resolution Manufacturing from 2D to 3D/4D Printing: Applications in Engineering and Medicine*, ed. S. L. Marasso and M. Cocuzza (Springer International Publishing, 2022), 17–46.

14. H. Kodama, "Stereoscopic Figure Drawing Device," Japanese Patent JPS56144478A, filed 12 April, and issued 10 November 1981, https://worldwide.espacenet.com/patent/search/family/012797030/publication/JPS56144478A?q=pn%3DJPS56144478A.

15. H. Kodama, "Automatic Method for Fabricating a Three-Dimensional Plastic Model with Photo-Hardening Polymer," *Review of Scientific Instruments* 52 (1981): 1770–1773, https://doi.org/10.1063/1.1136492.

16. E. Ueda, F. L. Geyer, V. Nedashkivska, and P. A. Levkin, "Droplet-Microarray: Facile Formation of Arrays of Microdroplets and Hydrogel Micropads for Cell Screening Applications," *Lab on a Chip* 12 (2012): 5218–5224, https://doi.org/10.1039/c2lc40921f.

17. P. G. Levkin and L. Florian, and U. U. Liebel, "Patterned Substrates for Cell Applications," European Patent EP2481794A1, filed 29 November 2010, and issued 23 August 2017, https://worldwide.espacenet.com/patent/search/family/043877338/publication/EP2481794B1?q=EP2481794B1.

18. P. Levkin, E. Boles, and F. Geyer, "Formation of Droplet or Hydrogel Arrays using Hydrophilic-Hydrophobic Patterned Surfaces for High-Throughput Screening Applications," European Patent EP2684601B1, filed 13 July 2012, and issued 20 November 2019, https://worldwide.espacenet.com/patent/search/family/046516497/publication/EP2684601B1?q=EP2684601B1.

19. L. J. Linxian, L. Junsheng, L. Pavel, D. Xin, and F. Wenqian, "Reactive Superhydrophobic Surfaces, Patterned Superhydrophobic Surfaces, Methods for Producing the Same and Use of the Patterned Superhydrophobic Surfaces," European Patent EP2952267B1, filed 5 May 2015 and issued 11 July 2018, https://worldwide.espacenet.com/patent/search/family/053054836/publication/EP2952267B1?q=EP2952267B1.

20. P. Levkin, F. Wenqian, and L. LI, "Patterned Substrate Having Hydrophilic and Hydrophobic Areas and Method for Producing the Same," European Patent EP3205394B1, filed 10 February 2016, and issued 10 January 2024, https://worldwide.espacenet.com/patent/search/family/055405090/publication/EP3205394B1?q=EP3205394B1.

21. P. Levkin, G. Michael, D. Zheqin, et al., "Patterned Substrate Having Hydrophilic and Hydrophobic Areas," European Patent EP3733277B1, filed 2 May 2019, and issued 21 February 2024, https://worldwide.espacenet.com/patent/search/family/066625742/publication/EP3733277B1?q=EP3733277B1.

22. M. Hartmann and S. Hardt, "Stability of Evaporating Droplets on Chemically Patterned Surfaces," *Langmuir* 35 (2019): 4868–4875, https://doi.org/10.1021/acs.langmuir.9b00172.

23. F. L. Geyer, E. Ueda, U. Liebel, N. Grau, and P. A. Levkin, "Superhydrophobic–Superhydrophilic Micropatterning: toward Genome-on-a-Chip Cell Microarrays," *Angewandte Chemie International Edition* 50 (2011): 8424–8427, https://doi.org/10.1002/anie.201102545.

24. E. Ueda, W. Feng, and P. A. Levkin, "Superhydrophilic–Superhydrophobic Patterned Surfaces as High-Density Cell Microarrays: Optimization of Reverse Transfection," *Advanced Healthcare Materials* 5 (2016): 2646–2654, https://doi.org/10.1002/adhm.201600518.

25. G. E. Jogia, T. Tronser, A. A. Popova, and P. A. Levkin, "Droplet Microarray Based on Superhydrophobic-Superhydrophilic Patterns for Single Cell Analysis," *Microarrays (Basel)* 5 (2016): 28, https://doi.org/10.3390/microarrays5040028.

26. D. D. Kartsev, E. Joaquin, J. E. U. Gomez, P. A. Anna, and P. A. Levkin, "Droplet Microarrays for Miniaturized and High-Throughput Experiments: Progress and Prospectives," *Advanced Materials Interfaces* 12 (2025): 2400905, https://doi.org/10.1002/admi.202400905.

27. X. Li, X. Zhang, S. Zhao, J. Wang, G. Liu, and Y. Du, "Micro-Scaffold Array Chip for Upgrading Cell-Based High-Throughput Drug Testing to 3D Using Benchtop Equipment," *Lab on A Chip* 14 (2014): 471–481, https://doi.org/10.1039/c3lc51103k.

28. J. Bruchmann, I. Pini, T. S. Gill, T. Schwartz, and P. A. Levkin, "Patterned SLIPS for the Formation of Arrays of Biofilm Microclusters with Defined Geometries," *Advanced Healthcare Materials* 6 (2016), https://doi.org/10.1002/adhm.201601082.

29. E. Boles, P. Levkin, U. Obst, T. Schwartz, and J. Li, "Use of Porous Hydrophobic Polymers Filled and Coated with Water Immiscible Hydrophobic Liquids for Protein- and Cell-Repellent Surfaces," European Patent EP2711417B1, filed 20 September 2012 and issued 9 November 2016, https://worldwide.espacenet.com/patent/search/family/047010142/publication/EP2711417B1?q=EP2711417B1.

30. A. B. D. Cassie and S. Baxter, "Wettability of Porous Surfaces," *Transactions of the Faraday Society* 40 (1944): 546, https://doi.org/10.1039/tf9444000546.

31. R. N. Wenzel, "Resistance of Solid Surfaces to Wetting by Water," *Industrial & Engineering Chemistry* 28 (1936): 988–994, https://doi.org/10.1021/ie50320a024.

32. H. Yu, D. Wang, X. Yang, et al., "Tailoring Protein Adsorption at the Solid–Liquid Interface for Long-Term Superhemophobicity," *Advanced Materials* 37 (2025): 2502388, https://doi.org/10.1002/adma.202502388.

33. Y. Wang, B. Zhang, H. Dodiuk, et al., "Effect of Protein Adsorption on Air Plastron Behavior of a Superhydrophobic Surface," *ACS Applied Materials & Interfaces* 13 (2021): 58096–58103, https://doi.org/10.1021/acsami.1c15981.

34. S. S. Melides, D. Vella, and M. Ramaioli, "Effect of Macroscopic Surface Heterogeneities on an Advancing Contact Line," *Langmuir* 38 (2022): 13358–13369, https://doi.org/10.1021/acs.langmuir.2c01026.

35. T.-S. Wong, S. H. Kang, S. K. Y. Tang, et al., "Bioinspired Self-Repairing Slippery Surfaces with Pressure-Stable Omniphobicity," *Nature* 477 (2011): 443–447, https://doi.org/10.1038/nature10447.

36. L. Xiao, J. Li, S. Mieszkin, et al., "Slippery Liquid-Infused Porous Surfaces Showing Marine Antibiofouling Properties," *ACS Applied Materials & Interfaces* 5 (2013): 10074–10080, https://doi.org/10.1021/am402635p.

37. G. Boveri, A. Corozzi, F. Veronesi, and M. Raimondo, "Different Approaches to Low-Wettable Materials for Freezing Environments: Design, Performance and Durability," *Coatings* 11 (2021): 77, https://doi.org/10.3390/coatings11010077.

38. DIN EN ISO/ASTM 52900. Additive Fertigung-Grundlagen-Terminologie. Berlin: Deutsches Institut für Normung (2022).

39. N. S. Allen, ed., *Photochemistry and Photophysics of Polymer Materials* (John Wiley & Sons, Inc, 2010).

40. E. M. Maines, M. K. Porwal, C. J. Ellison, and T. M. Reineke, "Sustainable Advances in SLA/DLP 3D Printing Materials and Processes," *Green Chemistry* 23 (2021): 6863–6897, https://doi.org/10.1039/d1gc01489g.

41. N. Corrigan, J. Yeow, P. Judzewitsch, J. Xu, and C. Boyer, "Seeing the Light: Advancing Materials Chemistry through Photopolymerization," *Angewandte Chemie International Edition* 58 (2019): 5170–5189, https://doi.org/10.1002/anie.201805473.

42. C. Yu, J. Schimelman, P. Wang, et al., "Photopolymerizable Biomaterials and Light-Based 3D Printing Strategies for Biomedical Applications," *Chemical Reviews* 120 (2020): 10695–10743, https://doi.org/10.1021/acs.chemrev.9b00810.

43. P. F. Jacobs, *Rapid Prototyping & Manufacturing: Fundamentals of Stereolithography*, (Society of Manufacturing Engineers, 1992).

44. "Bionova X Product Page," Cellink, accessed October 30, 2025, www.cellink.com/bioprinting/bionova-x.

45. J. R. Tumbleston, D. Shirvanyants, N. Ermoshkin, et al., "Continuous Liquid Interface Production of 3D Objects," *Science* 347 (2015): 1349–1352, https://doi.org/10.1126/science.aaa2397.

46. S. Iglauer, A. Salamah, M. Sarmadivaleh, K. Liu, and C. Phan, "Contamination of Silica Surfaces: Impact on Water–CO_2–Quartz and Glass Contact Angle Measurements," *International Journal of Greenhouse Gas Control* 22 (2014): 325–328, https://doi.org/10.1016/j.ijggc.2014.01.006.

47. T. Vukovic, J. Røstad, U. Farooq, O. Torsæter, and A. van der Net, "Systematic Study of Wettability Alteration of Glass Surfaces by Dichlorooctamethyltetrasiloxane Silanization—a Guide for Contact Angle Modification," *ACS Omega* 8 (2023): 36662–36676, https://doi.org/10.1021/acsomega.3c02448.

48. J. J. Cras, C. A. Rowe-Taitt, D. A. Nivens, and F. S. Ligler, "Comparison of Chemical Cleaning Methods of Glass in Preparation for Silanization," *Biosensors and Bioelectronics* 14 (1999): 683–688, https://doi.org/10.1016/s0956-5663(99)00043-3.

49. S. M. Losslein, R. Merz, D. W. Muller, M. Kopnarski, and F. Mucklich, "An in-depth Evaluation of Sample and Measurement Induced Influences on Static Contact Angle Measurements," *Scientific Reports* 12 (2022): 19389, https://doi.org/10.1038/s41598-022-23341-3.

50. T. Huhtamaki, X. Tian, J. T. Korhonen, and R. H. A. Ras, "Surface-Wetting Characterization Using Contact-Angle Measurements," *Nature Protocols* 13 (2018): 1521–1538, https://doi.org/10.1038/s41596-018-0003-z.

51. "PEGDA-INK Product Page," Cellink, accessed October 30, 2025, www.cellink.com/product/pegda-ink/.

52. M. Zhu, Y. Wang, G. Ferracci, J. Zheng, N.-J. Cho, and B. H. Lee, "Gelatin Methacryloyl and Its Hydrogels with an Exceptional Degree of Controllability and Batch-to-Batch Consistency," *Scientific Reports* 9 (2019): 6863, https://doi.org/10.1038/s41598-019-42186-x.

53. C. Claaßen, M. H. Claaßen, V. Truffault, et al., "Quantification of Substitution of Gelatin Methacryloyl: Best Practice and Current Pitfalls," *Biomacromolecules* 19 (2018): 42–52, https://doi.org/10.1021/acs.biomac.7b01221.

54. W. Feng, E. Ueda, and P. A. Levkin, "Droplet Microarrays: From Surface Patterning to High-Throughput Applications," *Advanced Materials* 30 (2018): 1706111, https://doi.org/10.1002/adma.201706111.

55. M. P. Schilling, S. Schmelzer, J. E. U. Gomez, A. A. Popova, P. A. Levkin, and M. Reischl, "Grid Screener: A Tool for Automated High-Throughput Screening on Biochemical and Biological Analysis Platforms," *IEEE Access* 9 (2021): 166027–166038, https://doi.org/10.1109/access.2021.3135709.

Supporting Information

Additional supporting information can be found online in the Supporting Information section.

Supporting File: adfm75212-sup-0001-SuppMat.pdf.